

# Reactivity imaging of a passive ferritic FeAlCr steel

Kirsten Agnes Lill · Koji Fushimi · Masahiro Seo ·  
Achim Walter Hassel

Received: 15 August 2007 / Revised: 7 April 2008 / Accepted: 7 April 2008 / Published online: 22 April 2008  
© The Author(s) 2008

**Abstract** A technique named reactivity imaging is introduced. It combines optical imaging of a polycrystalline material with orientation imaging by electron back scattering diffraction (EBSD) for a determination of the crystallographic orientation map and scanning electrochemical microscopy (SECM) for a visualization of the local reactivity. Dissolving metal ions from the substrate are directly detected by the scanning Pt tip of the SECM to measure the amount of locally dissolving material. A ferritic light weight steel (alloy Fe7.5Al7Cr) with a strong anisotropic dissolution behaviour was investigated as an example. This steel shows good passivation behaviour both, in air and through anodisation. In the passive state investigated here, the difference in dissolution rate between various crystallographic orientations is only marginal. Grain boundaries on the other hand showed a higher activity as compared to the grains themselves, which is attributed to the electronic tunnelling in the grain boundaries. The results demonstrate that the rate determining step responsible for the anisotropic dissolution does not result from a deficiency in passivation but from the active dissolution kinetics.

**Keywords** Steel · Scanning electrochemical microscopy · Electron back scatter diffraction · Grain dependence · Passivity

---

K. A. Lill · A. W. Hassel (✉)  
Max-Planck-Institut für Eisenforschung, Max-Planck-Str. 1,  
40237 Düsseldorf, Germany  
e-mail: hassel@elchem.de

K. Fushimi · M. Seo  
Graduate School of Engineering, Hokkaido University, Kita-13  
Jo, Nishi-8 Chome, Kita-ku, Sapporo 060-8628, Japan

## 1 Introduction

FeAlCr alloys are presently discussed as alternative steel qualities for special applications such as automotive exhaust pipes [1, 2]. For aluminium contents of up to about 7% a ferritic structure is achieved with high formability and deep drawability. In a former study it was found that Fe7.5Al7Cr exhibits remarkably strong anisotropic dissolution behaviour [3]. This behaviour immediately poses the question whether or not these differences are observed in the passive state of the material and to which extent the grain boundaries would contribute with a probably higher dissolution rate. The scanning droplet cell [4] that was used in this study [3] allows localising electrochemical techniques even to single grains of a material [5], to inclusions [6] or to single phases of a material [7]. The scanning electrochemical microscope (SECM) uses a different approach in which the localisation is achieved by a diffusion process rather by a strict separation of the electrode surface. This demonstrates that the method is capable of visualising the local electrochemical reactivity of a material [8]. Numerous investigations of the corrosion behaviour of various materials have been reported. Lee and Bard investigated surface oxide films on chromium and titanium and confirmed the insulating nature of these films [9]. Still and Wipf studied the breakdown of passive films on stainless steels [10] and acquired a distribution map of the oxidizable corrosion products from the surface. The localised corrosion of NiTi shape memory alloys was imaged by means of an alternating current scanning electrochemical microscope (AC-SECM) by Schulte et al. [11].

Martin and Unwin quantified the diffusion coefficient ratios of different redox couples demonstrating that they can be separated which is a prerequisite if a coupled chemical reaction has to be monitored [12]. Völker et al. monitored

the local flux of  $[\text{Fe}(\text{OH}_2)_6]^{2+}$  above the surface of low carbon steel coated with tin and an epoxyphenolic resin in tinfoil and chrome steel by employing the oxidation of  $[\text{Fe}(\text{OH}_2)_6]^{2+}$  to  $[\text{Fe}(\text{OH}_2)_6]^{3+}$  at a scanning Pt tip [13].

Fushimi et al. investigated the heterogeneity in thickness of passive films on pure iron by SECM [14] and presented differences in the dissolution behaviour on polycrystalline iron [15] and Fe–3Si [16]. Hassel et al. studied consecutive oxide formation on single grains of a polycrystalline titanium sample [17] which were produced by a scanning droplet cell [4]. The SECM was not only able to image oxide spots of various thicknesses on a single grain but also to recognise the structure of oxide spots with different ratios of potentiodynamically and potentiostatically formed oxides resulting from the sequence of oxide formation conditions [17, 18]. These studies prove that the SECM is the method of choice for the investigation of orientation dependent corrosion behaviour of materials.

The focus of this study is to investigate the heterogeneity of the passive films formed on Fe7.5Al7Cr in deaerated borate buffer solution pH = 8.4 with  $\text{K}_4[\text{Fe}(\text{CN})_6]$  as a mediator.

## 2 Experimental

### 2.1 Chemicals

All solutions were prepared from reagent grade chemicals and ultrapure water. A miniaturised Ag/AgCl/sat. KCl reference electrode was used [19]. Its potential was checked against a commercial type Ag/AgCl/sat. KCl reference electrode. A thin platinum wire with a diameter of 500  $\mu\text{m}$  and a purity of 99.999% was used as counter electrode. The FeAlCr working electrodes were prepared from high purity metals under an inert atmosphere. After casting, the alloy was heated in a nitrogen stream to 1,100  $^\circ\text{C}$ , rolled to a thickness of about 1–1.2 mm and finally heat treated in an inert Ar gas atmosphere with a residual oxygen concentration of 46 ppm for 24 h at 1,100  $^\circ\text{C}$  [3]. The chemical composition of the alloy as determined by material analysis using an ICP-OES (Inductively Coupled Plasma Optical Emission Spectrometer) is given in Table 1. The sample was ground with 600 and 1,000 grid paper. The grinding process was followed by finalising with 3 and 1  $\mu\text{m}$ -diamond slurries. The final step was a mixture of grinding and etching with an alkaline  $\text{SiO}_2$ -slurry with a particle size of 250 nm. Between the individual steps the sample has been

cleaned in deionised water, acetone and ethanol in an ultrasonic bath to remove residuals from the preparation processes. All potentials in the electrolyte are given versus the standard hydrogen electrode (SHE).

### 2.2 Platinum probe electrode and SECM

The probe electrode was a disc-shaped microelectrode composed of a platinum wire with a radius of 5  $\mu\text{m}$ , which was thermally sealed into a glass capillary. The tip of the probe electrode was mechanically ground with a microgrinder (EG-400, Narishige Co., Japan). For cleaning, cyclic voltammetry (CV) of the probe electrode was performed in the potential region between hydrogen evolution and oxygen evolution in 1 M  $\text{H}_2\text{SO}_4$  until the voltammogram did not change further.

A detailed description of the SECM setup used was given previously [15]. This system was additionally equipped with a force sensor to control the inter-electrode distance [16]. A probe electrode was located just above a specimen electrode and through the measurements of the probe current it detects the changes in activity of a redox reaction on the specimen electrode. By keeping the distance  $dz$  between the probe and the sample electrode constant while the probe electrode was scanned in the directions of the  $x$  and  $y$  axes, the probe current images are obtained, from which the heterogeneity of the specimen surface would be evaluated.

The probe electrode was scanned stepwise within a distance of 1,000  $\mu\text{m}$  in  $x$  direction with  $dx = 5 \mu\text{m}$  and an intermission of 0.2 s and 1,500  $\mu\text{m}$  in  $y$  direction with  $dy = 25 \mu\text{m}$  and an intermission of 0.5 s. The inter-electrode distance was constantly at  $dz = 15 \mu\text{m}$ . The total scan time for one map was 40 min.

### 2.3 Electron back scattering diffraction (EBSD)

The EBSD measurements were performed in a JSM6500F SEM (Jeol, Japan) with an EBSD detector (TSL). The tilting angle of the sample stage was  $70^\circ$ , acceleration voltage 15 kV and step size 50  $\mu\text{m}$ .

## 3 Results and discussion

### 3.1 Characterisation of the SECM

Figure 1 presents the CV of the micro electrode performed at a scan rate of  $dE/dt = 20 \text{ mV s}^{-1}$  in deaerated borate

**Table 1** Chemical composition of Fe7.5Al7Cr

	Al Wt%	C	Cr	Mo	N	Nb	O	P	S	Ti	Fe
Fe7.5Al7Cr	7.47	0.0008	6.98	<0.01	0.0178	<0.01	0.071	<0.01	0.0017	<0.001	Balance

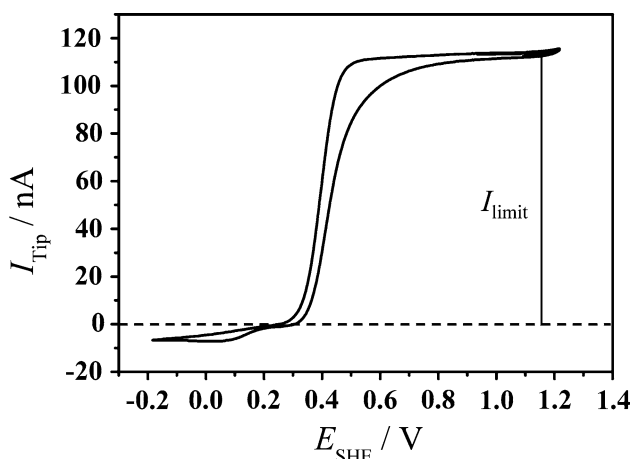


**Fig. 1** Cyclic voltammogram of the probe electrode measured in deaerated borate buffer solution pH = 8.4 containing 0.1 M  $[\text{Fe}(\text{CN})_6]^{4-}$  as mediator. The probe was far away from the sample surface. The scan rate was  $dE/dt = 20 \text{ mV s}^{-1}$

buffer solution of pH = 8.4 containing  $0.1 \text{ mol dm}^{-3}$   $\text{K}_4[\text{Fe}(\text{CN})_6]$  when the probe electrode is far from the sample surface. The CV has a sigmoidal shape with a diffusion-limiting current  $I_{\text{limit}} = 113 \text{ nA}$ . By using the following equation the radius  $a$  of the microelectrode can be calculated:

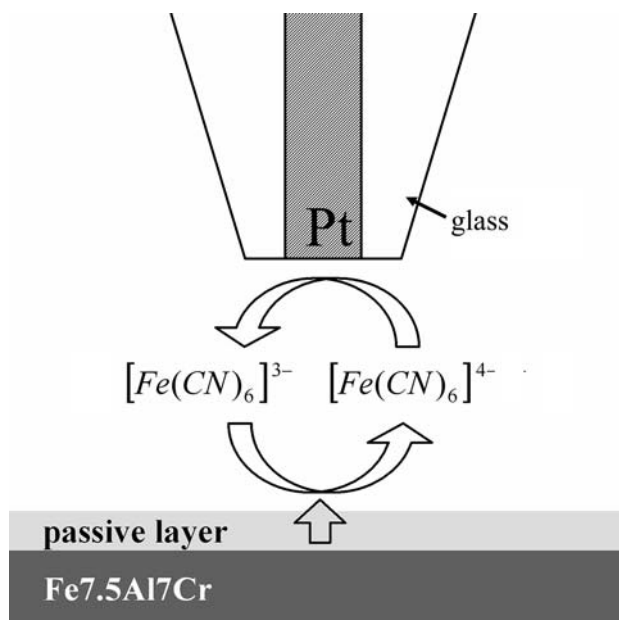
$$I_{\text{limit}} = 4nFDc^*a \tag{1}$$

where  $n$  is the number of electrons participating in the redox reaction,  $F$  the Faraday constant ( $96,485 \text{ A s mol}^{-1}$ ),  $D$  is the diffusion coefficient and  $c^*$  is the concentration of the electro active species in the bulk solution. By using  $D([\text{Fe}(\text{CN})_6]^{4-}) = 6.5 \times 10^{-10} \text{ m}^2 \text{ s}^{-1}$  [20] the radius  $a$  of the platinum micro electrode calculated from  $I_{\text{limit}}$  in Fig. 1 was  $4.5 \text{ }\mu\text{m}$ . This agrees well with the radius of  $5.0 \text{ }\mu\text{m}$  of the platinum wire employed for making the microelectrode.

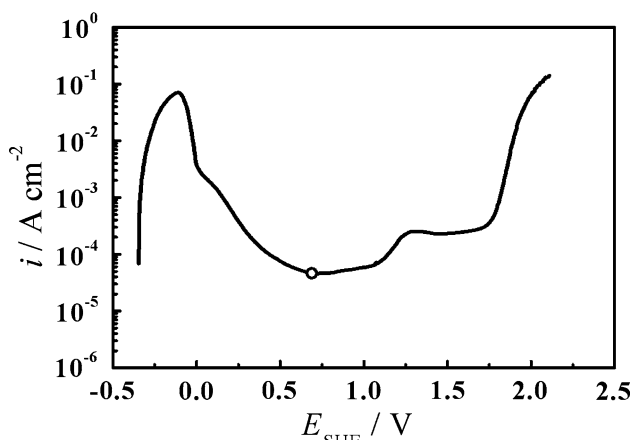
Figure 2 displays a schematic of the SECM operating mode used for the SECM measurements. In this measurement the SECM was used in the tip generation/substrate collection mode (TG/SC-mode) [6, 15–17]. The rate determining step was the electron transfer through the passive film.

Figure 3 shows the potentiodynamic scan of the alloy in  $0.5 \text{ M H}_2\text{SO}_4$  at a scan rate of  $dE/dt = 5 \text{ mV s}^{-1}$ . The circle (○) assigns the potential at which the sample has been passivated. Fe7.5Al7Cr shows the typical behaviour for a passivating material. Starting from the open circuit potential of  $-0.35 \text{ V}$  the transition from the active to the passive behaviour can be clearly seen. It is followed by a broad passive potential range from 0.5 to 1.1 V. The oxidation of  $\text{Cr}^{3+}$  to  $\text{Cr}^{6+}$  takes place between 1.1 and 1.73 V.

To passivate the sample, it was polarised for 1 h at a potential of  $0.7 \text{ V}$  in  $0.5 \text{ M H}_2\text{SO}_4$  according to the



**Fig. 2** Schematic of the tip generation/substrate collection mode on a passive electrode



**Fig. 3** Potentiodynamic scan of the alloy Fe7.5Al7Cr in  $0.5 \text{ M H}_2\text{SO}_4$  at a scan rate of  $dE/dt = 5 \text{ mV s}^{-1}$ . The cycle (○) assigns the potential at which the sample has been passivated

potentiodynamic behaviour represented in Fig. 3. The bipotentiostat was used as a potentiostat for this operation. After the passivation the electrolyte was removed and the cell, including the sample, was cleaned several times with doubly distilled water. The cell was then flushed with deaerated borate buffer solution containing  $0.1 \text{ M K}_4[\text{Fe}(\text{CN})_6]$  as mediator. Subsequently the cell was filled with this electrolyte. The potential of the probe electrode was controlled at  $E_P = 1.2 \text{ V}$  to oxidize  $[\text{Fe}(\text{CN})_6]^{4-}$  and the potential of the sample was controlled at  $E_S = 0 \text{ V}$  to reduce  $[\text{Fe}(\text{CN})_6]^{3-}$ .

### 3.2 Lateral resolution of the SECM measurements

To determine the lateral resolution of the SECM setup a circular platinum sample embedded into epoxy resin was used as a model specimen electrode. The model electrode was polarised at  $-0.1$  V while the micro electrode was polarised at  $0.9$  V in deaerated borate buffer solution of  $\text{pH} = 8.4$  containing  $0.1$  M  $\text{K}_4[\text{Fe}(\text{CN})_6]$ . This operation mode is known as TG/SC mode. The  $[\text{Fe}(\text{CN})_6]^{3-}$  is generated at the micro electrode due to the oxidation of  $[\text{Fe}(\text{CN})_6]^{4-}$  and then collected at the sample surface due to the reduction of the  $[\text{Fe}(\text{CN})_6]^{3-}$ . The schematic of this mode is given in Fig. 2. In this case however, the rate determining step is no longer the electron tunnelling through the thin passive layer rather the diffusion between tip and substrate.

Figure 4 represents the probe current image obtained when the probe electrode was scanned at  $dz = 15$   $\mu\text{m}$  over the sample surface with  $dx = 5$   $\mu\text{m}$  and  $dy = 25$   $\mu\text{m}$ . The total scan time for one map was 18 min. In Fig. 5 the probe current profile is displayed, which was obtained when scanning over the sample surface at the boundary of Pt and epoxy resin in  $x$  direction, indicated as the white dashed line in the lower right corner in Fig. 4. In order to determine the resolution of the Pt Tip from this scan vertical lines are drawn through the average value of the conducting area and that of the insulating area. In addition, a line is drawn through linear regression of the values as indicated by the line in Fig. 5. The lower limit was defined as a 15% increase of the current as compared to that over the insulating surface and the upper limit was set at the 85% level of the conducting substrates current level. The distance of these two points was calculated from a linear regression and the spatial resolution determined was  $40$   $\mu\text{m}$ .

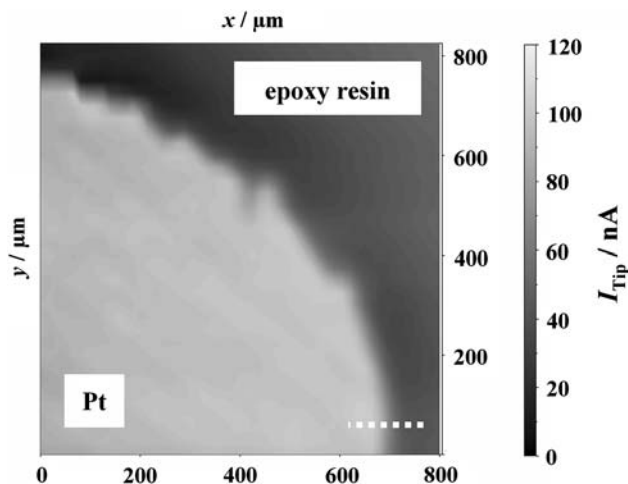


**Fig. 4** Probe current image obtained when the probe electrode was scanned over the model sample electrode surface

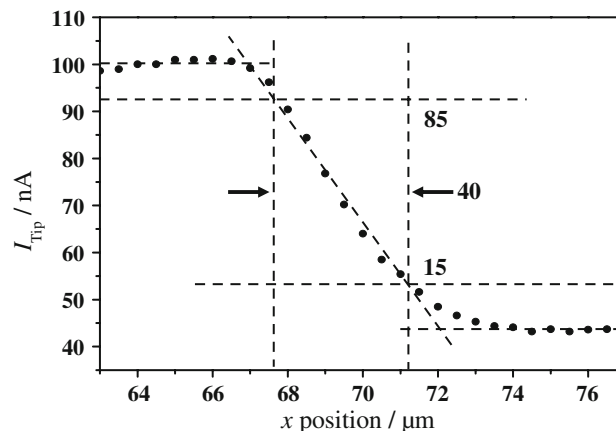


**Fig. 5** Probe current profile when the probe electrode was scanned along the dashed line drawn in the current image

### 3.3 Optical micrography

Figure 6 shows an optical micrograph of the sample prepared by the metallurgical procedure. A prominent, pentagon shaped grain can be seen in the centre, which has a diameter of about  $500$   $\mu\text{m}$  in the horizontal direction and about  $300$   $\mu\text{m}$  in the normal direction. The largest grain with some  $700$   $\mu\text{m}$  is seen at the upper rim of the image. Some smaller grains are also found which have a diameter

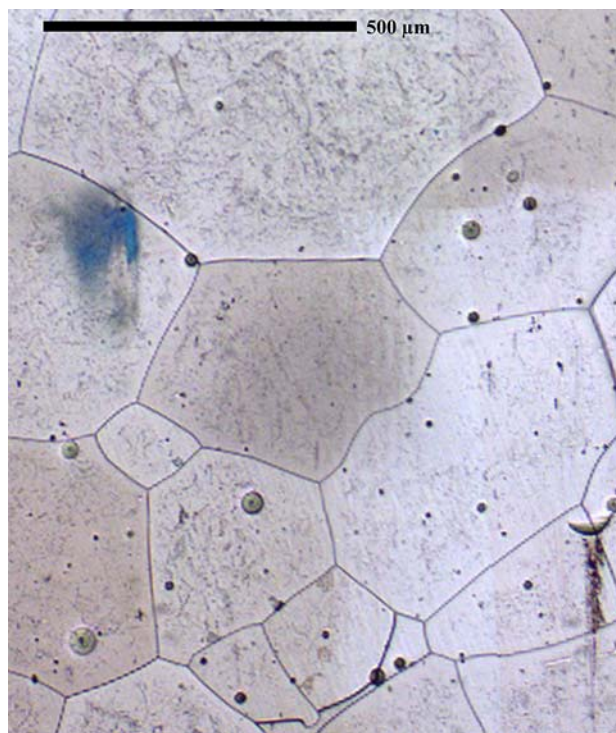


**Fig. 6** Optical micrograph of the sample after EBSD and SECM measurements. The semicircular indent in the right lower part of the picture was done after finishing the experiments to identify the investigated area

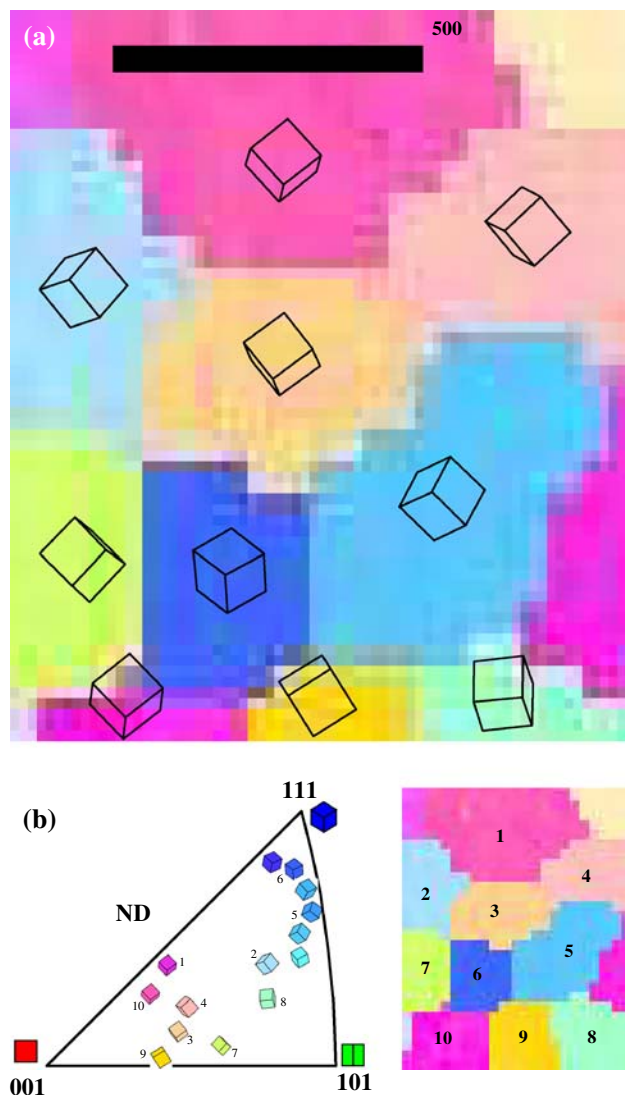


**Fig. 7** (a) EBSD map of the sample surface prior to the SECM measurement. The crystallographic orientation of the grains is represented by the cubes. (b) Correlation of the crystallographic orientation map and the inverse pole figure for the grains investigated in this study

of around 100  $\mu\text{m}$ . These large grains are a result of the special heat treatment.

### 3.4 Electron back scattering diffraction

Figure 7a shows an EBSD map of the same area as in Fig. 6. The pattern found in the optical micrograph can be recognized in the EBSD map. Comparing the shape of the grains it is seen that the grain boundaries appear a bit fuzzy. This is a result of the step size of 50  $\mu\text{m}$  for the orientation determination. The classification of the crystallography was performed based on a grain tolerance angle of  $5^\circ$  and a minimum grain size of 50  $\mu\text{m}$ . The phase used for indexing the Kikuchi pattern was iron ( $\alpha$ ). The crystallographic

orientation of the single grains is represented by the cubes in the EBSD map. The orientation can be also seen in the colour encoding of the inverse pole (Fig. 7b).

The results demonstrate that the heat treatment leaves a representative selection of crystallographic orientations. There are orientations near the elementary planes (001), (101) and (111). Moreover, also higher indexed planes remain after the annealing procedure, e.g. the centre pentagon shaped grain. Other materials such as gold can not be processed in this simple way since the surface energy differences of the various crystallographic planes are too large. This causes growth of the close-packed and low surface energy (111) plane under consumption of other orientations. This results in a heavily textured, polycrystalline material with azimuthally rotated (111) grains, that is no longer representative for a typical polycrystalline material [5].

For the material investigated here this does not happen and therefore ensures a proper representation of the various crystallographic orientations. Prior to the EBSD mapping shown here an indexing of the Kikuchi pattern was performed with various crystal phases but with a lower spatial resolution. In each case, the  $\alpha$ -Fe phase received the lowest error and therefore the highest probability, demonstrating that the material was purely ferritic. Subsequently, scans were performed with higher resolution, which were indexed using the above mentioned parameters.

### 3.5 SECM map of the passive sample surface

Figure 8 shows the probe current image measured after the Fe7.5Al7Cr sample surface was passivated for 1 h at 0.7 V. It is seen from the comparison between Figs. 6, 7 and 8 that the shapes of the grains in the probe current image coincide completely with the shapes of the grains in the EBSD map and that on the optical image. The semi-circular indent in the right lower part of the optical picture was produced after finishing the experiments, in order to allow an easier recognition of the investigated area. As mentioned before, there are representatives for various crystallographic orientations. A comparison of the probe current distributions measured on the single grains show only a weak dependency on the crystallographic orientation. For example, the pentagon shaped central grain is slightly higher than the large grain at the upper rim of the image. However, the differences between the grains are marginal. This can be seen not only in Fig. 8 but also in Table 2 in which current values for some representative points, indicated by small numbers in Fig. 8, are listed. Points 4, 6 and 8 refer to different crystallographic orientations. Points 2, 5 and 7 are representatives for grain boundaries and Points 1 and 3 were chosen as triple points of grain boundaries.

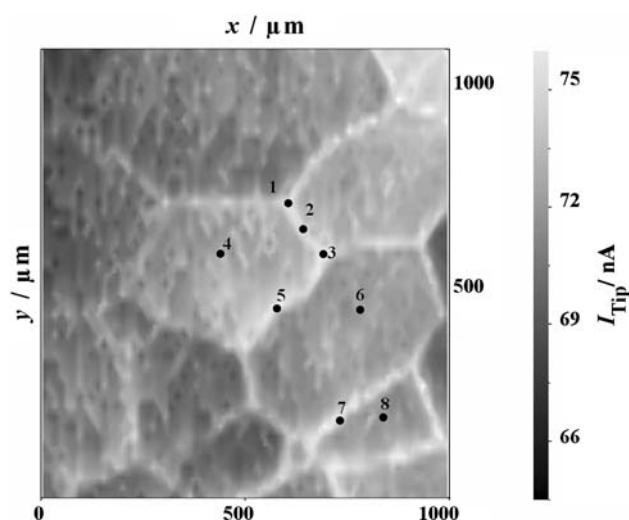


**Fig. 8** Probe current image measured in deaerated borate buffer solution pH = 8.4 containing 0.1 M  $[\text{Fe}(\text{CN})_6]^{4-}$  as mediator after the Fe7.5Al7Cr sample was passivated in 0.5 M  $\text{H}_2\text{SO}_4$  solution for 1 h at 0.7 V. The probe electrode was polarised to 1.2 V while the sample was polarised to 0 V. Some representative points in the map where selected and indicated by the small numbers 1–8 in this figure. See text (Sect. 3.5) for details

**Table 2** Tip current values extracted from SECM map in Fig. 8 in the passive state

Position	Point	$I_{\text{tip}}/\text{nA}$
Triple	1	74.6
Boundary	2	74.5
Triple	3	75.4
Grain	4	71.8
Boundary	5	74.9
Grain	6	71.4
Boundary	7	75.1
Grain	8	71.2

The SECM is indirectly detecting the tunnelling of electrons through the thin passive layers of the oxide films. This tunnelling is very sensitive to differences in the oxide film thickness. The height of the tunnel barrier on the other side can influence the rate to a similar degree. This barrier height might result from small composition differences between oxides on different crystallographic orientation of the substrate. This can also influence the relative permittivity of the material and therefore the Debye length. On the other side, the height differences of substrate grains will play no role since the rate determining step is the transport through the passive film and not the diffusion of the species from the tip to the substrate.

The grain boundaries on the other hand show a much higher activity than the grains themselves. This can be also seen from Table 2. This activity could be the result of a

crystallographic distortion at the adjacent grains. In principle, a different chemical composition might be discussed that results from a segregation of impurities into the grain boundary. However, scanning Auger and ToF-SIMS analysis did not show such enrichment but demonstrated that the passive film forming on all grains consisted mainly of aluminium and chromium oxides [21]. As for the grains the SECM measurement can not distinguish between a lower barrier height and a thinner film in the grain boundary. Nevertheless, the effect is quite strong as seen in Fig. 8. Present studies which make use of an advanced and automated scanning droplet cell [22, 23], will complement these investigations by a full electrochemical characterisation. Furthermore does a combined SECM/EBSD study during passive to active transition reveal the differences in the increase of the reaction rates for different crystallographic orientations [21]?

#### 4 Summary

In this study the corrosion behaviour of the ferritic light weight steel Fe7.5Al7Cr was investigated in the passive regime. This alloy with its passivating components Al and Cr exhibits pronounced passivity. By means of a SECM operated in tip generation substrate collection mode with  $\text{K}_4[\text{Fe}(\text{CN})_6]$  as mediator the reactivity of a polycrystalline sample was imaged. It is found that this method is well suited to correlate the crystallographic microstructure of the material to its conductivity.

The reactivity of different grains is almost identical, giving no explanation for the strongly anisotropic dissolution behaviour of the material. The grain boundaries on the other hand were found to show increased conductivity. Comparison of the optical micrograph and the EBSD map shows that the optically visible grains are of significantly different crystallographic orientation representing the entire range of orientations. A SECM map of exactly this area allows direct correlation of the optical appearance, the crystallographic structure and the reactivity. This is mainly due to the fact, that the grain boundaries, which are recognised in the optical image and in the EBSD map as boundaries between the grains, are even more pronounced in the SECM map. They appear as white lines of higher reactivity between the darker grains.

**Acknowledgements** K. A. Lill thanks the *Japanese Society for the Promotion of Science (JSPS)* for financial support of this work through a short term fellowship. The authors thank G. Frommeyer for providing the FeCrAl steel.

**Open Access** This article is distributed under the terms of the Creative Commons Attribution Noncommercial License which permits any noncommercial use, distribution, and reproduction in any medium, provided the original author(s) and source are credited.

## References

1. Brück U, Frommeyer G, Jimenez J (2002) *Steel Res* 73:543
2. Echsler H, Martinez EA, Singheiser L, Quadackers WJ (2004) *Mat Sci Eng A* 384:1
3. Lill KA, Hassel AW, Frommeyer G, Stratmann M (2005) *Electrochim Acta* 51:978
4. Hassel AW, Lohrengel MM (1997) *Electrochim Acta* 42:3327
5. Hassel AW, Seo M (1999) *Electrochim Acta* 44:3769
6. Vignal V, Krawiec H, Heintz O, Oltra R (2007) *Electrochim Acta* 52:4994
7. Rao VS, Kwon HS (2007) *J Electrochem Soc* 154:C255
8. Eckhard K, Chen XX, Turcu F, Schuhmann W (2006) *Phys Chem Chem Phys* 8:5359
9. Lee C, Bard AJ (1990) *Anal Chem* 62:1906
10. Still JW, Wipf DO (1997) *J Electrochem Soc* 144:2657
11. Schulte A, Berger S, Etienne M, Schuhmann W (2004) *Mat Sci Eng A* 378:523
12. Martin RD, Unwin PR (1998) *Anal Chem* 70:276
13. Völker E, Gonzáles Inchauspe C, Calvo EJ (2006) *Electrochem Commun* 8:179 and Erratum, *Electrochem Commun* 8:909
14. Fushimi K, Azumi K, Seo M (1999) *ISIJ Int* 39:346
15. Fushimi K, Seo M (2001) *Electrochim Acta* 47:121
16. Fushimi K, Lill KA, Habazaki H (2007) *Electrochim Acta* 52:4246
17. Hassel AW, Fushimi K, Okawa T, Seo M (1999) *Electrochem Soc Proc PV* 99-28:166
18. Hassel AW, Fushimi K, Seo M, in preparation
19. Hassel AW, Fushimi K, Seo M (1999) *Electrochem Commun* 1:180
20. Adams RN (1969) *Electrochemistry at solid electrodes*. Marcel Dekker Ltd, New York
21. Lill KA, Fushimi K, Seo M, Stratmann M, Hassel AW, in preparation
22. Lill KA, Hassel AW (2006) *J Solid State Electrochem* 10:941
23. Mardare AI, Wieck AD, Hassel AW (2007) *Electrochim Acta* 52:7865